THE INVESTIGATIONS AND 2-D COMPUTATIONS OF ELECTROMAGNETIC FIELDS AND FORCES DISTRIBUTION OF SQUIRREL CAGE INDUCTION MOTOR WITH BROKEN END RINGS

H. H. HANAFY **Tamer M. ABDO** **Amr A. ADLY**
hanafy_hassan@hotmail.com. tam2k0@gmail.com. amradly@ieee.org.
Electrical Power & Machines Department, Faculty of Engineering, Cairo University, Giza, 12613, Egypt

***Abstract**: In this paper an ABC transient model of the three phase induction motor is developed that depends on self and mutual inductance calculations based on accurate 2D finite element analysis (FEA). This model can represent both healthy and faulty motor conditions. The rotor broken end rings faults are studied thoroughly including their effects on the motor speed, motor torque, rotor bars and end ring currents distribution. Flux distribution and the forces exerted on the rotor bar are also studied. Broken end rings causes non-uniform distribution of the rotor bar currents which will lead to fluctuations in the motor torque and speed. Also it results in non-uniform radial forces affecting the bars which will increase the mechanical stresses on the rotor shaft and bearings.*

***Keywords:** induction motor, finite element analysis, broken end rings.*

1. Introduction

Induction motors are the most used motor in industrial and domestic applications. They are rugged, mechanically simple, easy to maintain and simple to control. Motor electrical faults are divided into stator and rotor faults. One of the rotor faults are broken end ring fault. This fault is mostly caused by manufacturing defects and maintenance procedures. For detailed and accurate analysis of motor performance in faulty conditions, an accurate model for the motor in which all conditions can be considered is of great importance. In [1], basic methods for faulty induction motor modeling have been reviewed such as magnetic equivalent circuit method, finite different method, winding function method, and finite-element method (FEM). A detailed steady state model was developed to simulate rotor cage and unbalanced voltage faults in [2-3]. FEM has been introduced as one of the most comprehensive modeling methods. FEM was used to accurately calculate the steady state equivalent circuit parameters of the induction motor in [4-5]. The parameters for a two-axis model suitable for dynamic analysis were calculated using finite-element analysis (FEA) [6-7]. A finite element-state space coupled (CFE-SS) model with iterative solution was developed in [8], where it was used to obtain the dynamic performance of the induction motor. Time-stepping finite element method (TS-FEM) coupled with circuit and mechanical equations were successfully used to analyze the transient and steady state performance [9-10]. In [11] the broken end rings fault was discussed using extended park vector approach. In [12] the transient analysis and simulation for broken bars and end rings were developed using machine parameters calculated from FEM. TS-FEM was used to study broken end rings fault among other rotor faults in [13]. In [14], the effects of broken end ring fault on the torque-speed characteristics of the motor were discussed.

This paper presents a study for the performance of induction motor using an ABC transient model with self and mutual inductances calculated from a commercial FEM software package. The motor is analyzed under healthy and under various broken end ring fault conditions. The cases of healthy rotor, one broken end ring, two adjacent broken end rings and two non-adjacent broken end rings are studied. The motor performance including the stator, bars and end rings currents, the developed torque and the motor speed is discussed. The current density in the bars, the magnetic flux density distribution and the force exerted on the bars are also analyzed. It was found that the non-uniform distribution of the bar currents that was caused by the broken end ring segments, will cause fluctuations in the motor torque and speed, which increase as the number of broken segments increases. On the other hand, the radial forces are non-uniform causing mechanical stresses on the motor shaft and bearings.

2. Motor Parameters Calculations

It is well known that the stator windings of the induction motor are divided into three symmetric phases and that the cage rotor constitutes bars that are interconnected with two rings, one from each side. It can be assumed that the current in the rotor flows in loops where each rotor loop is formed of two bars and two ring segments as shown in Fig. 1.

The self and mutual inductances of the motor are calculated using 2D model for the induction motor. The model has been analyzed – by utilizing a commercially available package – using the finite element method (FEM) where non-linear magnetic characteristics were taken into account.

The flux linking with the stator phases or the rotor loops can be calculated from the vector magnetic potential as given:

$$\phi = \oint \bar{A}.\bar{dl} \tag{1}$$

To calculate the self and mutual inductance for stator phases, the model is solved with only one energized stator phase. The self-inductance will be:

$$L_{s\,ii} = \frac{\phi_{ii}}{I_i}, \tag{2}$$

where i = 1, 2 or 3 and ϕ_{ii} is the flux linking the phase number i due to current in the same phase. While the mutual inductance is calculated using:

$$M_{s\,ij} = \frac{\phi_{ij}}{I_i}, \tag{3}$$

where i & j= 1 , 2 or 3 and ϕ_{ij} is the flux linking the phase number j due to current in phase number i.

The stator self and mutual inductances can be expressed as follows:

$$L_s = l_s + L_{os}, \tag{4}$$

$$M_s = -\frac{L_{os}}{2}, \tag{5}$$

where l_s is the stator leakage inductance and L_{os} is the stator magnetizing inductance.

The self-inductance of rotor loops can be calculated in a similar manner and expressed as follows:

$$L_r = l_r + L_{or}, \tag{6}$$

While the mutual inductance, considering only the fundamental component, can be expressed as follows:

$$M_{rhm} = L_{or}\cos\big((h-m)\alpha\big), \tag{7}$$

where h & m = 1, 2, … N_b refers to a rotor cage loop number ($h \neq m$), l_r is the rotor leakage inductance, L_{or} is the rotor magnetizing inductance and α is the rotor slot pitch.

It should be pointed out that the mutual-inductances between stator phases and rotor loops are rotor-position-dependent. Hence, the following stator to rotor approximate mutual-coupling, considering only the fundamental component, expression may be adopted:

$$M_{nm} \approx L_{osr}\cos\left(\theta \pm k\frac{2\pi}{3} + (m-1)\alpha\right), \tag{8}$$

where, k = 0, 1 or 2, n = a, b or c denotes a particular stator phase and L_{osr} is the maximum mutual coupling.

The stator winding resistance is calculated using the relation:

$$r_s = \frac{N_s l_{mt}}{\sigma A_c}, \tag{9}$$

where N_s is the number of turns per phase, l_{mt} is the turn mean length, σ is the conductivity of copper and A_c is the conductor cross section area.

The rotor bar and end ring segment resistances are calculated from the following equations.

$$r_b = \frac{l_b}{\sigma A_b}, \tag{10}$$

$$r_e = \frac{2\pi D_r \rho}{N_b\, t(D_r - D_i)} K_{ring} \tag{11}$$

where, l_b is the bar length, A_b is the bar cross section area, , D_i is the inner ring diameter, D_r is the diameter at the middle of the bar, N_b the number of bars, t is the ring height and K_{ring} is a correction factor given in [15].

The rotor parameters are referred to the stator side using the effective turns-ratio.

$$a = \frac{N_s K_{ws}}{N_r K_{wr}}, \tag{12}$$

where

$$K_{ws} = \sin\left(\frac{\theta_s}{2}\right) * \frac{\sin\left(\frac{q\alpha_s}{2}\right)}{q\sin\left(\frac{\alpha_s}{2}\right)}, \tag{13}$$

$$K_{wr} = \sin\left(\frac{\alpha}{2}\right), \tag{14}$$

where, N_r is the number of turns of the rotor loop, θ_s is the stator coil span angle, q is the number of slots per pole per phase, and α_s is the stator slot pitch.

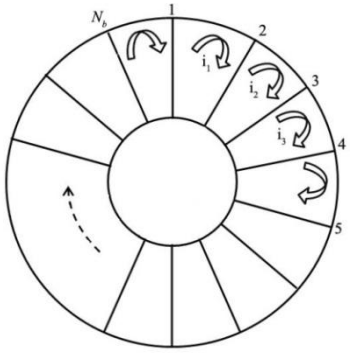

Fig. 1. Schematic Diagram for the rotor loops (formed by the bars and end rings) showing the rotor loop currents.

3. Induction Motor Modeling

The voltage differential equations correlating the induction motor voltages and currents may be expressed in the form:

$$\begin{bmatrix} V_s \\ V_r \end{bmatrix} = \begin{bmatrix} R_{ss} + pL_{ss} & pL_{sr} \\ pL_{rs} & R_{rr} + pL_{rr} \end{bmatrix} \begin{bmatrix} I_s \\ I_r \end{bmatrix}, \quad (15)$$

where $p = \frac{d}{dt}$, while R_{ss}, R_{rr}, L_{ss}, L_{rr} and $L_{sr} = L_{rs}^T$ are given in matrix form as shown below:

$$R_{ss} = \begin{bmatrix} r_s & 0 & 0 \\ 0 & r_s & 0 \\ 0 & 0 & r_s \end{bmatrix}, \quad (16)$$

$$R_{rr} = \begin{bmatrix} r_L & -r_b & 0 & \bullet\bullet\bullet & 0 & -r_b \\ -r_b & r_L & \bullet & & & 0 \\ 0 & \bullet & \bullet & \bullet & & \bullet \\ \bullet & & \bullet & \bullet & \bullet & 0 \\ 0 & & & \bullet & \bullet & -r_b \\ -r_b & 0 & \bullet\bullet\bullet & 0 & -r_b & r_L \end{bmatrix}, \quad (17)$$

$$r_L = 2r_b + 2r_e, \quad (18)$$

$$L_{ss} = \begin{bmatrix} L_s & M_s & M_s \\ M_s & L_s & M_s \\ M_s & M_s & L_s \end{bmatrix}, \quad (19)$$

$$L_{rr} = \begin{bmatrix} L_r & M_{r12} & M_{r13} & \bullet & M_{r1N_b} \\ M_{r12} & L_r & \bullet & & \\ M_{r13} & \bullet & \bullet & \bullet & \bullet \\ \bullet & & \bullet & \bullet & \\ \bullet & & & \bullet & \\ M_{r1N_b} & \bullet & \bullet & & L_r \end{bmatrix}, \quad (20)$$

$$L_{sr} = L_{rs}^{\ T} = \begin{bmatrix} M_{a1} & M_{a2} & M_{a3} & \bullet\bullet\bullet & M_{aN_b} \\ M_{b1} & M_{b2} & & \bullet\bullet\bullet & M_{bN_b} \\ M_{c1} & \bullet\bullet\bullet & & & M_{cN_b} \end{bmatrix}. \quad (21)$$

It should be mentioned that the above matrices could be modified in accordance with the different fault conditions. In case of broken end rings, the loop containing the broken ring is considered an open circuit as shown in Fig. 2. This can be simulated by increasing the resistance of the broken segment. The resistance of the broken segment in this analysis is considered to be 1000 times its original value.

For simplicity, (15) may be written in the form:

$$V = (R + pL)I. \quad (22)$$

By re-arranging (22) to incorporate rotor motion we get:

$$V = RI + LpI + \omega_r \frac{dL}{d\theta} I, \quad (23)$$

$$pI = L^{-1}V - L^{-1}\left(R + \omega_r + \frac{dL}{d\theta} \right) I, \quad (24)$$

Moreover, expressions for the developed torque (T_e), mechanical equation of motion and force acting on the m^{th} rotor bar $\overline{F}_m$ in terms of its current density ($\overline{J}$) and flux density ($\overline{B}$) acting on it may be given by the expressions:

$$T_e = \frac{1}{2} I^T \frac{dL}{d\theta} I, \quad (25)$$

$$T_e - T_L = \frac{J}{P} \frac{d\omega_r}{dt}, \quad (26)$$

$$\overline{F}_m = l_b \iint_{S_{bar}} \left(\overline{J}_c \times \overline{B} \right) dS, \quad (27)$$

where T_L is the load torque and J is the motor moment of inertia, P is the number of per poles and l_b is the bar length.

It turns out that equations (24)-(26) may be collectively dealt with as an initial value problem (IVP). Once this IVP problem is solved, currents in the stator phases and the rotor loops may be determined for a given load torque and specific motor parameters.

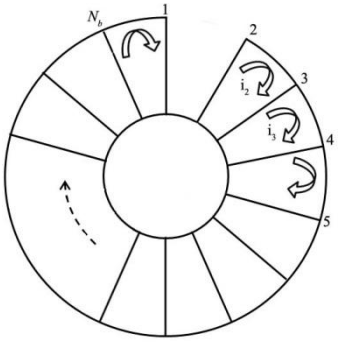

Fig. 2. Schematic Diagram for the rotor loops (formed by the bars and end rings) showing the rotor loop currents in case of one broken end ring.

4. Simulation Results

A 5.5 kW, 380 volts, 4-pole, 48 stator slots and 28 rotor bars induction motor was used to perform the analysis. Sample simulation results for four cases are demonstrated below. In specific, simulation results for the cases of; healthy rotor, one broken end ring,

two adjacent broken end rings and two non-adjacent broken end rings are demonstrated.

For healthy rotor case the currents in the rotor end rings are similar and the currents in the bars are also similar as shown on Fig. 3 and 4. While in the case of one broken end ring (end segment of rotor loop 1 as shown in Fig. 2), the end ring currents are no longer similar as shown in Fig. 5. The end ring currents in the ring segments adjacent to the broken one and in a ring segment away from the broken one are shown. The peak current in the end rings adjacent to the broken end ring has decreased compared to the healthy case while in the end ring away from the broken one the current is almost the same as the healthy case. As a result, the bar currents adjacent to the broken end ring segment are not similar as shown in Fig. 6. The peak bar current of the bar before the broken end ring decreased while the one after increased compared to the healthy case. Similar results are obtained for the case of two adjacent broken end rings, which are segments of rotor loops 1 and 2, as shown in Fig.7 and 8. An increase in the peak bar current in the bar after the broken end rings is noticed compared to the one broken end ring case. The case of two non-adjacent broken end rings, which are end ring segments of rotor loops 1 and 14, is shown in Fig. 9 and 10. The bar currents in the bars adjacent to the two broken end rings behaves similarly to previous broken end ring cases.

The motor torque and speed at the different cases described above are shown in Fig. 11 and 12 respectively. It's obvious that there are fluctuations in the motor torque in the different cases of broken end ring which results in fluctuations in the motor speed. As the number of broken end ring increases, the average torque decreases and the fluctuations worsens.

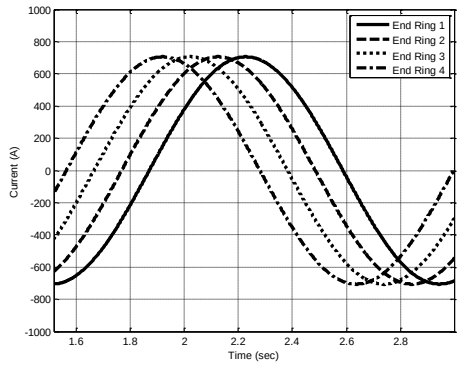

Fig. 3. End ring currents for healthy rotor at rated conditions.

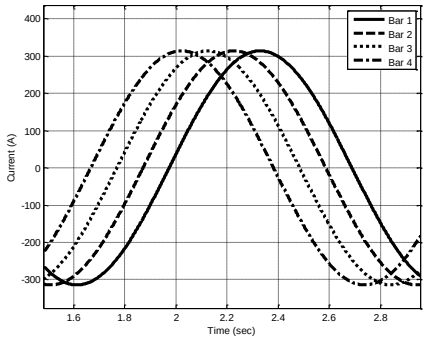

Fig. 4. Bar currents for healthy rotor at rated conditions.

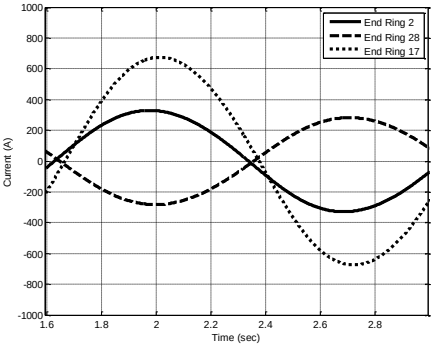

Fig. 5. End ring currents for the case of one broken end ring at rated conditions.

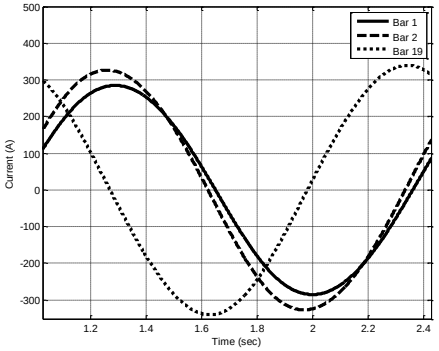

Fig. 6. Bar currents for the case of one broken end ring at rated conditions.

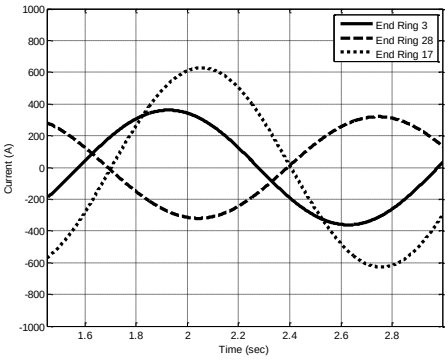

Fig. 7. End rings currents for the case of two adjacent broken end rings at rated conditions.

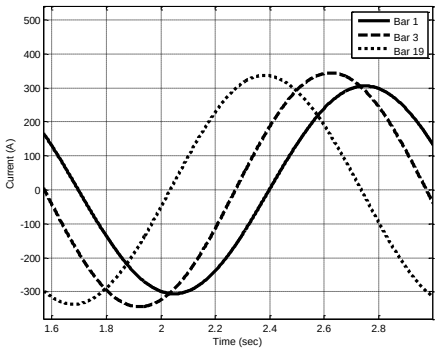

Fig. 8. Bar currents for the case of two adjacent broken end rings at rated conditions.

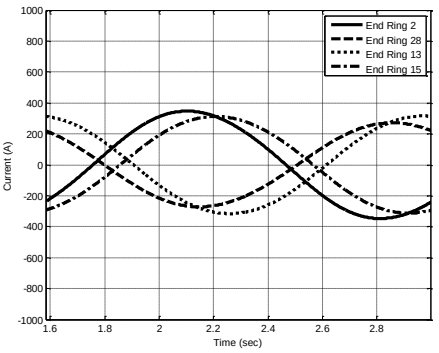

Fig. 9. End rings currents for the case of two non-adjacent broken end rings at rated conditions.

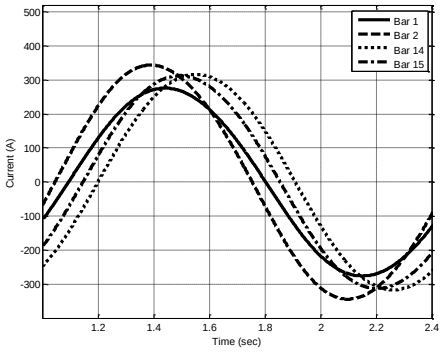

Fig. 10. Bar currents for the case of two non-adjacent broken end rings at rated conditions.

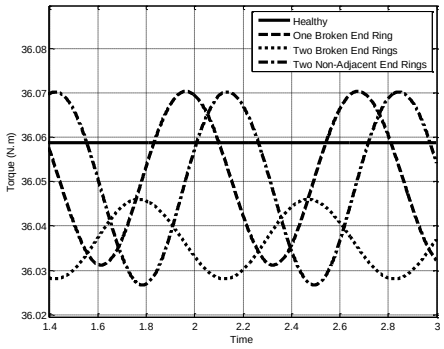

Fig. 11. The motor torque at different cases at rated conditions.

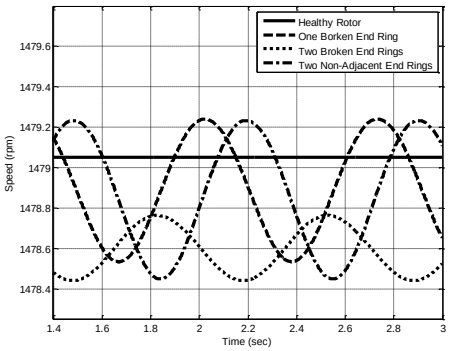

Fig. 12. The motor speed at different cases at rated conditions.

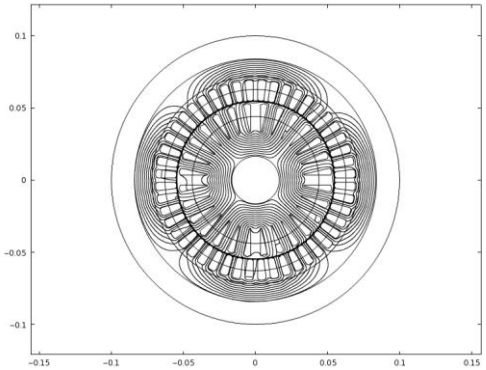

Fig. 13. Magnetic flux density distribution for a healthy rotor at an arbitrary chosen instant.

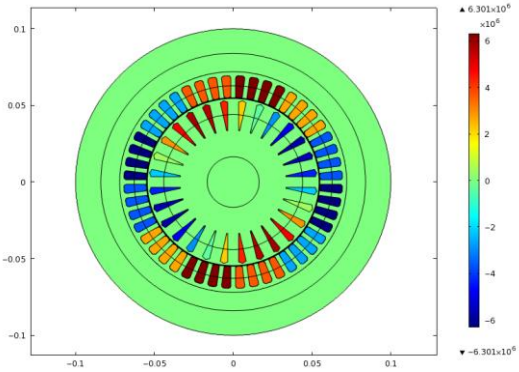

Fig. 14. Current density distribution in stator phases and rotor bars for healthy rotor at the same instant of Fig. 13.

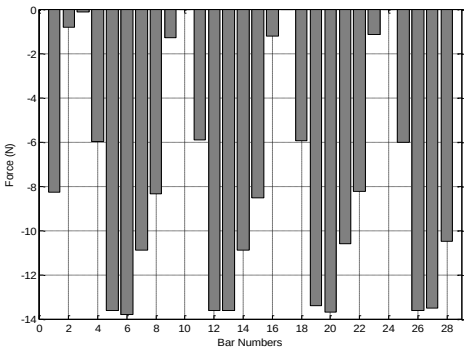

Fig. 15. Radial forces for healthy rotor at rated conditions at the same instant of Fig.13.

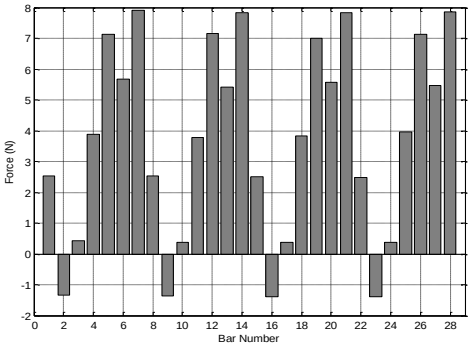

Fig. 16. Tangential forces for healthy rotor at rated conditions at the same instant of Fig. 13.

Forces affecting each bar were calculated using the same FEM software that was used to calculate the inductances. For all cases the tangential and radial forces are calculated at an instant where the current in phase 'a' is maximum.

The magnetic flux density distribution and current density distribution for a healthy rotor is shown in Fig. 13 and 14, respectively. The radial and tangential are shown in Figs. 15 and 16, respectively. It can be seen from these figures that, for the case of healthy rotor, the radial forces are almost symmetric and cancel each other. On the other hand, the tangential forces, which are responsible for generating the motor torque, are symmetrical under the machine poles.

The magnetic flux density distribution and current density distribution for the case of one broken end ring are shown in Fig. 17 and 18, respectively. Distributions of the tangential and radial forces corresponding to the same instant are shown in Fig. 19 and 20, respectively. It can be observed from Fig. 19 that the radial forces are asymmetrical in this case, leading to a net radial force affecting the rotor shaft and, eventually, the bearings. Moreover, the tangential forces are no longer symmetric under the machine poles as shown in Fig. 20. The negative tangential forces cause a decrease in the average torque compared to the healthy case.

Moreover, distributions for the magnetic flux density and current density in case of two adjacent broken end rings are shown in Fig. 21 and 22, respectively. The tangential and radial forces are shown in Fig. 23 and 24, respectively. It can be observed from Fig. 23 that the asymmetry in the radial forces has increased in comparison to the case of one broken end ring. Such increase in the asymmetry would negatively affect the bearings life time.

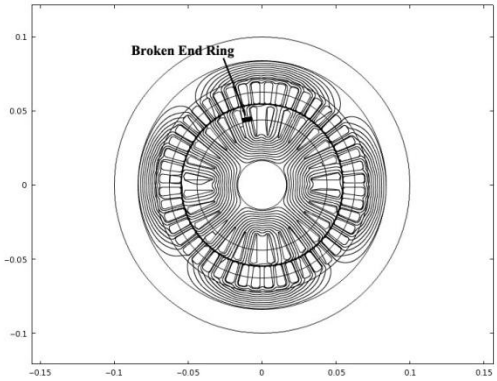

Fig. 17. Magnetic flux density distribution for one broken end ring shown in black at an arbitrary chosen instant.

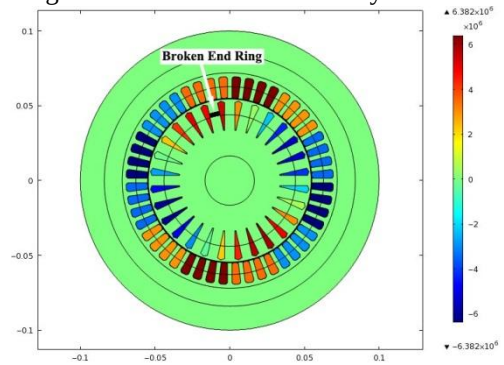

Fig. 18. Current density distribution in stator phases and rotor bars for one broken end ring shown in black at the same instant of Fig. 17.

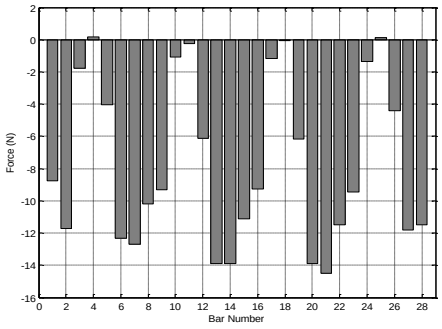

Fig. 19. Radial forces for one broken end ring at rated conditions at the same instant of Fig.17.

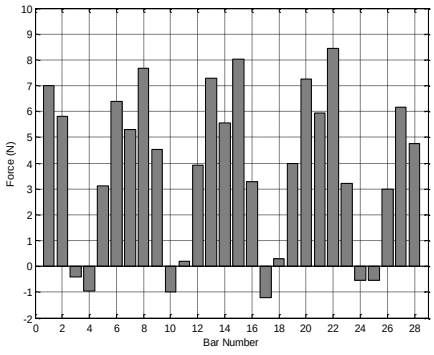

Fig. 20. Tangential forces for one broken end ring at rated conditions at the same instant of Fig.17.

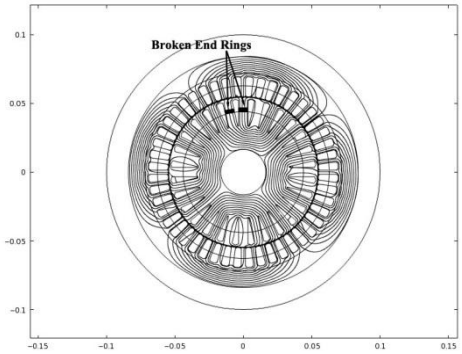

Fig. 21. Magnetic flux density distribution for two adjacent broken end rings shown in black at an arbitrary chosen instant.

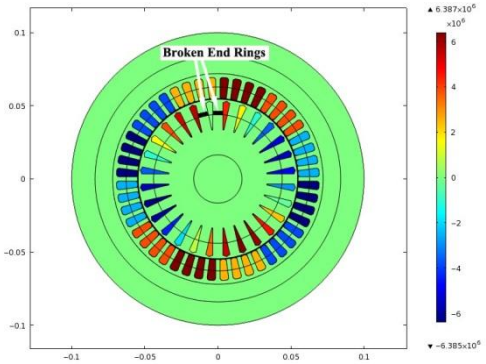

Fig. 22. Current density distribution in stator phases and rotor bars for two adjacent broken end rings shown in black at the same instant of Fig. 21.

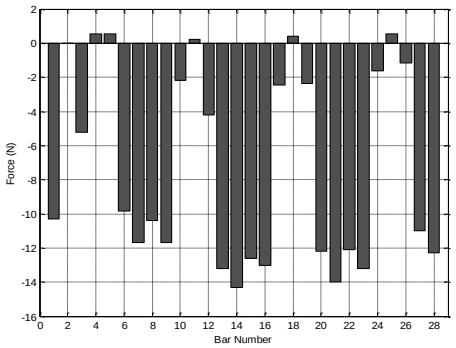

Fig. 23. Radial forces for two adjacent broken end rings at rated conditions at the same instant of Fig.21.

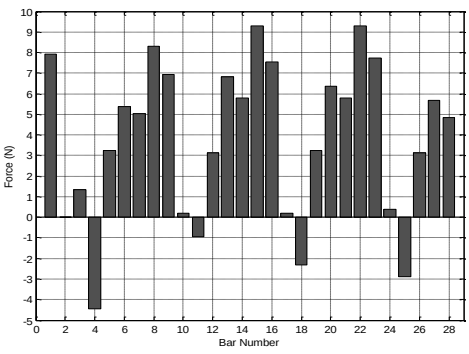

Fig. 24. Tangential forces for two adjacent broken end rings at rated conditions at the same instant of Fig.21.

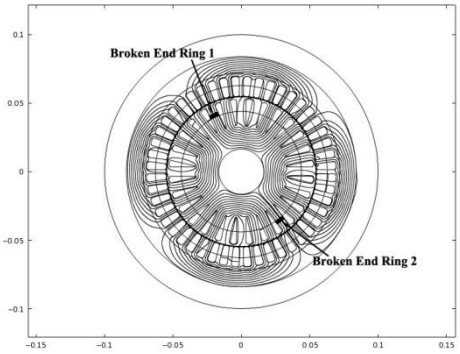

Fig. 25. Magnetic flux density distribution for two non-adjacent broken end rings shown in black at an arbitrary chosen instant.

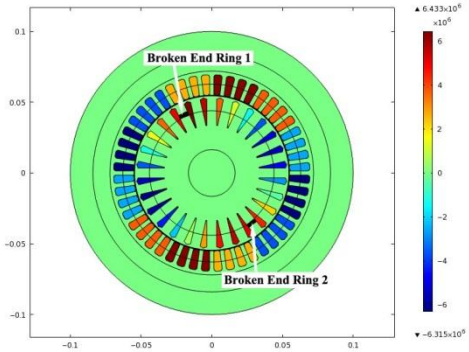

Fig. 26. Current density distribution in stator phases and rotor bars for two non-adjacent broken end rings shown in black at the same instant of Fig.25.

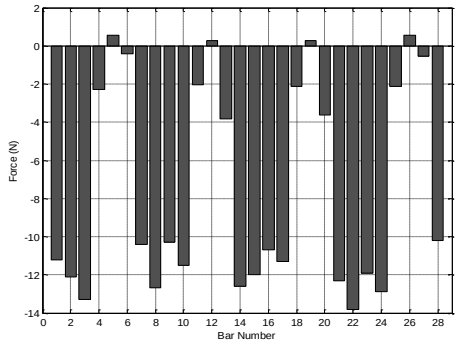

Fig. 27. Radial forces for two non-adjacent broken end rings at rated conditions at the same instant of Fig.25.

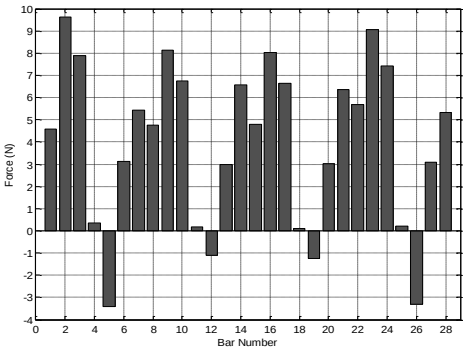

Fig. 28. Tangential forces for two non-adjacent broken end rings at rated conditions at the same instant of Fig.25.

Increased asymmetry of the tangential forces, as illustrated by Fig. 24, would result in increased torque and speed variations. The negative tangential forces cause a decrease in the average torque compared to the healthy case. Similar results for the case of two non-adjacent broken end rings are shown in Fig. 25-28.

It can be seen from the magnetic flux density distributions, shown in Fig. 13, Fig. 17, Fig. 21 and Fig. 25, that the distribution in the faulty cases are asymmetric compared to the healthy case.

5. Conclusions

This paper presents an efficient model to analyze broken end rings fault conditions for induction motors using a FEM approach coupled with an ABC transient model. The pattern of the asymmetry in bar and end ring currents resulted from various broken end ring faults can be deduced and analyzed. Effects on the motor torque and speed can be detected. Using the proposed approach it is possible to asses instantaneous radial and tangential force asymmetries resulting from single or multiple broken end ring conditions. The proposed approach may be utilized in predicting the net mechanical stresses on the motor shaft and bearings which may lead to motor eccentricity and bearing faults as a result of rotor faults. Deterioration in motor performance may also be assessed.

References

1. Faiz J., Ebrahimi B.M., Sharifian M.B.B.: *Different faults and their diagnosis techniques in three-phase squirrel-cage induction motors—a review.* In: Electromagnetics, XVI (2006), No.7, Aug. 2006, p.543- 569.
2. Abdel-Hamid M.N., El-Markabi M.H., Adly A.A.: *Operation of Cage Induction Motor with Unbalanced Voltages and Rotor Cage*. In: Proceedings of the Middle East Power Systems Conference MEPCON ‘89**,** Jan. 9-13, 1989, Cairo, Egypt, p.139-145.
3. Williamson S., Smith A.C.: *Steady-state analysis of 3-phase cage motors with rotor-bar and end-ring faults*. In: IEE Proceedings on Electric Power Applications, CXXIX (1982), No. 3, May 1982.
4. Yamazaki K., Suzuki A., Ohto M., Takakura T., Nakagawa S.: *Equivalent circuit modeling of induction motors considering stray load loss and harmonic torques using finite element method.* In: IEEE Transactions on Magnetics, XLVII (2011), No. 5, May 2011, p.986–989.
5. Nerg J., Pyrhönen J., Partanen J.: *Finite element modeling of the magnetizing inductance of an induction motor as a function of torque*. In: IEEE Transactions on Magnetics, XL (2004), No. 4, July 2004, p.2047–2049.
6. Gmiden M.H. , Trabelsi H.: *Calculation of two-axis induction motor model using Finite Elements with coupled circuit.* In: Proceeding of the 6th International Multi-Conference on Systems, Signals and Devices, March 23-26, 2009, Djerba, Tunisia, p.1- 6.
7. Dolinar D., De Weerdt R., Belmans R., Freeman E.M.: *Calculation of two-axis induction motor model parameters using finite elements*. In: IEEE Transactions on Energy Conversion, XII (1997), No. 2, June 1997, p.133–142.
8. Demerdash N.A., Baldassari P.: *A combined finite element-state space modeling environment for induction motors in the ABC frame of reference the no-load condition*. In: IEEE Transactions on Energy Conversion, VII (1992), No. 4, Dec. 1992, p.698–709.
9. Vassent E., Meunier G., Foggia A., Reyne G.: *Simulation of induction machine operation using a step by step finite element method coupled with circuits and mechanical equations.* In: IEEE Transactions on Magnetics, XVII (1991), No. 6, Nov. 1991, p.5232–5234.
10. Degeneff R.C., Gutierrez M.R., Salon S.J., Burow D.W., Nevins R.J., *Kron’s reduction method applied to the time stepping finite element analysis of induction machines.* In: IEEE Transactions on Energy Conversion, X (1995), No. 4, Dec. 1995, p.669–674.
11. Aboubou A., Sahraoui M., Zouzou S.E., Razik H., Rezzoug A.: *Broken bars and/or end rings detection in three-phase induction motors by the extended Park's vector approach.* In: Proceedings of the 9th IEEE International Power Electronics Congress, Oct. 17-22, 2004, Celaya, Mexico, p. 128-133.
12. Kang M., Huang J.: *Simulation and analysis of squirrel cage induction machines under rotor internal faults.* In: Proceedings of the 8th International Conference on Electrical Machines and Systems ICEMS ‘05, Sept. 27-29, 2005, Nanjing, China, Vol. III, p.2023-2027.
13. Bangura J.F., Demerdash N.A.: *Effects of broken bars/end-ring connectors and airgap eccentricities on ohmic and core losses of induction motors in ASDs using a coupled finite element-state space method.* In: IEEE Transactions on Energy Conversion, XV (2000), No. 1, Mar. 2000, p.40-47.
14. Arabacı H., Bilgin O.: *Effects of rotor faults in squirrel-cage induction motors on the torque-speed curve.* In: Proceedings of the 19th International Conference on Electrical Machines ICEM ‘10, Sept. 6-8, 2010, Rome, Italy, p.1-5.
15. Williamson S.: *Calculation of the resistance of induction motor end rings*. In: IEE Proceedings on Electric Power Applications, CXXXIII (1986), No. 2, March 1986, p.54-60.